Ultramicroscopy 111 (2011) 1262–1267

Contents lists available at ScienceDirect

Ultramicroscopy

journal homepage: www.elsevier.com/locate/ultramic

Exploring different inelastic projection mechanisms for electron tomography

B. Goris *, S. Bals, W. Van den Broek, J. Verbeeck, G. Van Tendeloo

EMAT, University of Antwerp, Groenenborgerlaan 171, B-2020 Antwerp, Belgium

ARTICLE INFO

Article history:
Received 10 December 2010
Received in revised form
10 February 2011
Accepted 22 February 2011
Available online 1 March 2011

Keywords:
Electron tomography
EFTEM
Thickness map
Plasmon map

ABSTRACT

Several different projection mechanisms that all make use of inelastically scattered electrons are used for electron tomography. The advantages and the disadvantages of these methods are compared to HAADF–STEM tomography, which is considered as the standard electron tomography technique in materials science. The different inelastic setups used are energy filtered transmission electron microscopy (EFTEM), thickness mapping based on the log-ratio method and bulk plasmon mapping. We present a comparison that can be used to select the best inelastic signal for tomography, depending on different parameters such as the beam stability and nature of the sample. The appropriate signal will obviously also depend on the exact information which is requested.

1. Introduction

Nanosystems within the field of physics, biology and chemistry are becoming smaller and more complex from a structural as well as from a chemical point of view. As a consequence, higher demands are being put to microscopic and nanoscopic characterisation techniques. Transmission electron microscopy images yield valuable information about the structure and the chemical composition of nanostructured materials. The disadvantage of these methods is that they only provide two dimensional (2D) images of three dimensional (3D) objects. However, knowledge of the 3D structure and composition is indispensable to understand the physical properties of these nanostructures in comparison to their bulk counterparts. For example, it is known that the melting point of Au nanoparticles with a 2.5 nm diameter is ~40% lower than that of bulk Au [1]. A precise determination of the morphology of nanometre sized particles is therefore important to optimise specific size and/or shape dependant properties. Electron tomography is a technique to create a 3D reconstruction from a tilt series of TEM images and has been used for the first time in the 1960s for a 3D study of biological macromolecules [2,3]. However, bright field TEM images of crystalline samples are influenced by unwanted diffraction contrast caused by the elastic scattering of the incoming electron beam. Therefore, the so-called 'projection requirement', which states that an image signal must be a monotonic function of a physical property of the object [4] is not fulfilled. To overcome this problem, high angle annular dark field (HAADF) scanning transmission electron microscopy (STEM) images are often used for electron tomography. However, also images created by different imaging techniques can be suitable for 3D reconstruction.

In the past, several different projection methods that all make use of *inelastically* scattered electrons have already been used for electron tomography. The most commonly known inelastic form of electron tomography is based on energy filtered transmission electron microscopy (EFTEM). This type of tomography uses chemical sensitive elemental maps or jump ratio maps as projections and was introduced in 2001 by Möbus and Inkson [5] and Möbus et al. [6]to study Y_2O_3 particles in polycrystalline FeAl. The technique has also been used to obtain a 3D reconstruction of the backbone in a magnetotactic bacteria [7,8] and to study FeNi nanoparticles [9]. A different form of EFTEM tomography, where single energy loss images are used as projections is used to study complex polymers [10]. Bulk plasmon maps taken at low energy losses are already used as projections for tomography to study the 3D shape of multiwall C nanotubes [11] and for the study of Si nanoparticles [12]. Although electron tomography can be performed using different inelastic imaging techniques [13], it is often unclear which technique is best suited for a given problem.

In this work, we will not only study the advantages and the disadvantages of 3D EFTEM and bulk plasmon mapping, also the use of thickness maps (based on inelastic electrons) is proposed and investigated for electron tomography. In addition, we will make a comparison with HAADF–STEM, which is often considered as the standard electron tomography technique in materials science [14]. Our results will provide useful information concerning the selection of the optimal inelastic signal for electron tomography depending on the specific material and depending on the information required.

* Corresponding author. Tel.: +32 3 265 32 46; fax: +32 3 265 33 18.
E-mail address: bart.goris@ua.ac.be (B. Goris).

0304-3991/$ - see front matter © 2011 Elsevier B.V. All rights reserved.
doi:10.1016/j.ultramic.2011.02.007

2. Experimental techniques

HAADF–STEM images, which are often used for electron tomography in materials science, are formed by collecting scattered electrons using an annular detector with a high inner collection angle (>60 mrad). Electron beams scattered by the specimen to such high angles conform closely to Rutherford's scattering law stating that the scattered intensity is proportional to the square of the atomic number and proportional to the specimen thickness [15].

We will compare the results of HAADF–STEM tomography with different TEM modes, all using inelastically scattered electrons. These techniques include EFTEM tomography, thickness map tomography and bulk plasmon tomography.

EFTEM is generally considered as the most useful technique for inelastic electron tomography. In this work, both elemental maps created using the three window method and jump ratio maps based on the jump ratio method [16] are used as an input for 3D reconstruction. In an elemental map, the resulting intensity per pixel is proportional to the number of electrons that made a specific excitation.

We also present a novel and more straightforward approach towards inelastic electron tomography using thickness maps based on the log-ratio method [16]. These maps can be created by taking the logarithm of the ratio of a BF-TEM image and a zero-loss filtered image. The intensity present in the thickness maps is equal to the thickness of the specimen expressed in units of the inelastic mean free path.

Another technique to acquire projections that can be used for 3D reconstruction is using bulk plasmon maps. These maps can be obtained by inserting a small energy slit around the bulk plasmon peak in the EELS spectrum. When neglecting elastic effects, such as diffraction contrast, bulk plasmon maps fulfil the projection requirement, since the scattering probability scales with the sample thickness up to a value where multiple scattering has to be taken into account (± 100 nm) [17].

HAADF–STEM images as well as the EFTEM, thickness and bulk plasmon maps are acquired using a Jeol 3000 F, operating at 300 kV, equipped with a Gatan Imaging Filter (GIF 2000 with a $1k \times 1k$ CCD camera). The inner collection angle of the HAADF-detector corresponds to 60 mrad. The alignment of the tilt series and the 3D reconstructions are carried out using the FEI Inspect3D software.

3. Results

3.1. EFTEM tomography

In order to compare the results of an EFTEM tomography experiment with a HAADF–STEM 3D reconstruction, a test sample existing of a C nanohorn surrounding a Cu core is used. More information on the preparation of these samples can be found in [18] and in Fig. 1 a 2D TEM and a STEM image of the nanohorn are presented.

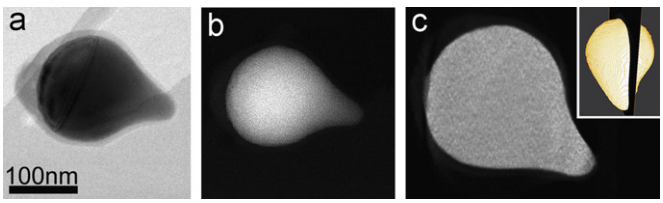

Fig. 1. (a) TEM image of a C nanohorn with a Cu core. (b) 2D HAADF–STEM projection from the nanohorn. Because of the high contrast difference between C and Cu, only the Cu core of the nanohorn is visible. (c) An orthoslice which reveals a uniform density of the Cu core in the nanohorn. The slice through the reconstruction is chosen as indicated on the voltex visualisation in the inset of image (c).

The HAADF–STEM series is recorded over a tilt range of $\pm 70^\circ$ with an increment of 2°. A 3D reconstruction is obtained using the SIRT algorithm [19]. The inset in Fig. 1c shows a voltex visualisation of the reconstructed volume in which the specific morphology of the Cu core can be clearly recognised. An orthoslice through the 3D reconstruction is presented in Fig. 1c and shows uniform intensity values, which confirms a homogenous composition of the Cu core. The C shell surrounding the core (as can be observed in TEM, Fig. 1a) is not clearly visible in the 3D reconstruction because of the large contrast difference between Cu and C in the individual HAADF–STEM projections.

An EFTEM tilt series is acquired over a tilt range of $\pm 70^\circ$ with an increment of 5°. For each tilt angle, six energy loss images are acquired, 3 for the Cu $L_{2,3}$-edge (811, 891 and 971 eV) and 3 for the C K-edge (250, 272 and 298 eV). An energy slit width of 20 eV and an acquisition time of 3 s per energy loss image is used for C, whereas a width of 50 eV in combination with an acquisition time of 40 s per energy loss image is used for Cu. Spatial drift between the two pre-edges and the post-edge is corrected using cross-correlation. Elemental maps generated with a regular three window method and jump ratio maps are obtained both for Cu and C. Examples are shown in Fig. 2. Remaining diffraction contrast is still obvious in the elemental maps, which is expected to violate the projection requirement. This diffraction contrast can be partially removed using the ratio of an elemental map and a zero-loss image [20], but this approach might cause other artefacts because image resolution also changes as a function of energy-loss [21].

In principle, diffraction contrast should be strongly reduced in jump ratio maps, but contrast can still be present caused by changes of the diffraction contrast itself as a function of energy. The jump ratio maps are found to contain more noise at positions outside the sample. The resulting Cu and C maps are spatially aligned manually with respect to each other prior to the following alignment steps in the reconstruction process. The alignment of the tilt series is first carried out using the Cu map tilt series since this series had the highest signal to noise ratio (SNR). Next, this

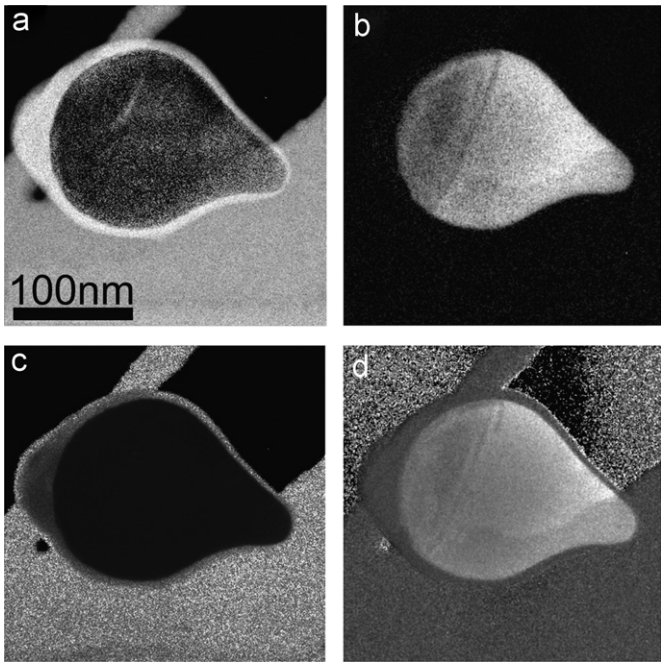

Fig. 2. Elemental maps of carbon (a) and copper (b) created using the three window method. (c) and (d) show a jump ratio map using the jump ratio method. The elemental maps suffer more from diffraction contrast, but the jump ratio map has a lower signal to noise ratio.

alignment is transferred to the C map tilt series, which can be expected to have an identical alignment.

3D reconstructions are made using the SIRT algorithm for both the elemental and jump ratio maps. The result for the elemental maps is shown in Fig. 3a, where voltex visualisations of the Cu and the C reconstruction are presented. This figure shows a good agreement between both morphologies. As seen from the ortho-slice through the 3D reconstruction (Fig. 3c and e), the intensity in the reconstructed Cu core is not as uniform as compared to the HAADF–STEM reconstruction. This is also clear from the intensity profile which is obtained along the direction indicated by the white arrow in Fig. 3e. This effect is most likely caused by the combination of diffraction contrast present in the elemental maps and the multiple scattering of electrons in the thicker central part of the particle.

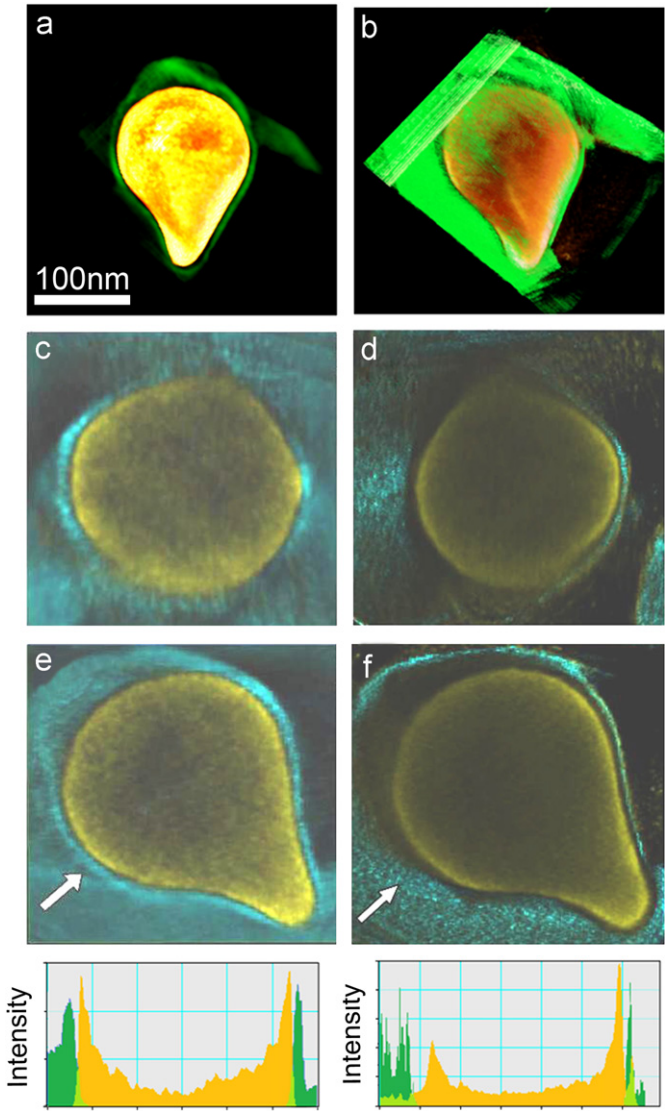

Fig. 3. Reconstruction based on a tilt series of elemental maps created by the three window technique (a,c,e) and jump ratio maps (b,d,f). (a) and (b) show a voltex visualisation of the reconstruction of a C nanohorn with a Cu core. (c)–(f) show orthoslices through the reconstructed volumes. The reconstructed morphology of the three window method corresponds to the morphology reconstructed with HAADF–STEM tomography. The orthoslices through the reconstructed volume clearly show that the intensity at the centre of the Cu core is lower than the intensity at the edge of the Cu core. This effect is caused by the diffraction contrast in the elemental maps and is also shown in the intensity profile through the orthoslice. A lower signal to noise ratio is observed for the reconstruction based on the jump ratio maps in comparison to the reconstruction of the three window method. The morphology of the C shell is not very well reconstructed due to the limited validity of the projection requirement in the jump ratio maps. The intensity profiles are chosen in the direction of the white arrows in (e) and (f).

The result for the jump ratio maps is illustrated in Fig. 3b, d and f, where a voltex visualisation and orthoslices through the reconstructions are shown. Both the voltex rendering and the orthoslices show a lower signal to noise ratio in comparison to the reconstruction based on elemental maps obtained through the three window method. In addition, the morphology of the C shell is not very well reconstructed. This can be explained based on the limited validity of the projection requirement in jump ratio maps. The projection requirement is not fulfilled because most of the thickness information is lost by applying a division in the jump ratio method since both the ionisation-edge signal as the background signal depend linearly on the thickness of the specimen. Because the energy-loss background intensity rises faster as a function of thickness than the ionisation-edge signal [22], thicker areas may even give rise to a lower intensity in the jump ratio map.

3.2. Thickness map tomography

A simple and straightforward approach to inelastic electron tomography is the use of thickness maps. The method is based on the use of the log-ratio model. This model states that the thickness of a specimen can be determined in units of the inelastic mean free path λ of the electrons [23] which means that these maps are suitable as projections in a tomographic tilt series. The log-ratio formula is given by $t/\lambda = \log(I_{tot}/I_0)$ where I_{tot} and I_0 are the total and zero-loss areas under the electron energy loss spectrum, respectively. In practise, a thickness map can be generated by taking the ratio of a TEM image and a zero-loss filtered image. The division of the TEM image by the zero-loss image partly removes diffraction contrast as well. The technique does not require a specific crystalline structure and can be applied within a wide thickness range ($\sim$15–500 nm) until multiple scattering starts to play an important role [24,25]. Here, bamboo-like C nanotubes are investigated [26]. A tilt series is acquired over $\pm 70^\circ$ with an angular increment of 2°. For each tilt angle, a BF-TEM image and a zero-loss image are acquired. The zero-loss image is acquired by centering a 5 eV energy slit around the zero-loss peak. The spatial drift between both images is corrected using cross-correlation and a thickness map is generated for every tilt angle.

Fig. 4a shows a thickness map of a bamboo-like C nanotube acquired at zero tilt angle. A reconstruction is made using a SIRT algorithm and the result is shown in Fig. 4b, in which a voltex visualisation from the C nanotube is presented. The bamboo-like structure with cavities inside the nanotube is also clearly visible in Fig. 4c, which shows an orthoslice through the reconstruction. This example clearly illustrates the potential of the method when 3D reconstruction of the morphology is required. In order to evaluate whether chemically sensitive reconstructions can be obtained, a tilt series is acquired for a Mn_3O_4 octahedrical

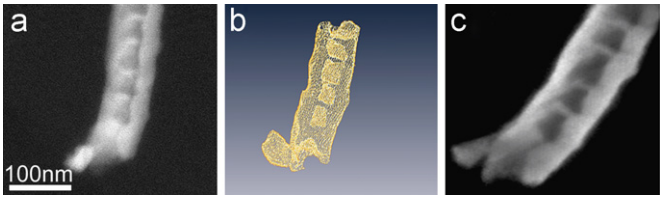

Fig. 4. (a) Thickness map of a C nanotube with a bamboo-like structure. (b) A voltex visualisation of the reconstruction of the C nanotube based on the thickness map tilt series. The morphology of the C nanotube is visible and also the bamboo-like structure is shown. (c) An orthoslice of the nanotube.

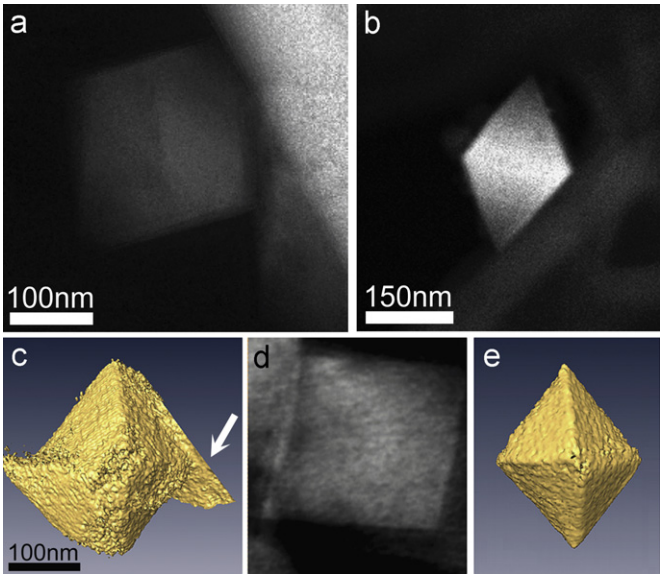

Fig. 5. (a) A thickness map of a Mn_3O_4 octahedron on a carbon grid at a zero tilt angle. (c) Reconstruction of the Mn_3O_4 octahedron on a carbon grid based on the thickness map tilt series. The white arrow indicates the carbon grid on which the octahedron is attached. At the opposite side of the octahedron, the beginning of a second particle is also visible. As can be seen from the orthoslice in (d), no intensity difference is noticeable between a voxel containing Mn_3O_4 and a voxel containing carbon. (b) HAADF–STEM projection from another Mn_3O_4 octahedron. (e) 3D reconstruction based on this HAADF–STEM tilt series which confirms the octahedral morphology of the nanoparticles [28].

nanoparticle supported on a carbon grid. Here, the tilt angle is $\pm 70^\circ$ and the tilt interval is 2°. A reconstruction is made using the SIRT algorithm and the result is shown in Fig. 5. The carbon support layer and the Mn_3O_4 nanoparticles cannot be distinguished. The reason is that the inelastic mean free path of electrons is almost identical for most compounds [27]. Consequently, there is only little contrast between the Mn_3O_4 octahedron and the C layer.

3.3. Plasmon tomography

At low energy-loss values (5–50 eV), the electron energy loss spectrum is dominated by the plasmon peak caused by the inelastic scattering of electrons at the bulk and surface plasmon modes of the sample. Bulk plasmon tomography is demonstrated here using an Al needle-shaped sample. This sample, prepared by focused ion milling, is mounted on a dedicated tomography holder which is able to tilt over 360° [29,30]. A 2D image from the bulk plasmon modes is obtained using a small energy slit centred at an energy loss equal to the bulk plasmon energy of the specimen. 2D projections are collected over a tilt range of $\pm 90^\circ$ and an interval of 5° between two successive projections is used. The acquisition is done using the EFTEM-spectrum imaging (EFTEM-SI) technique by which an image series is acquired using adjacent energy intervals [31]. The image with an energy-loss corresponding to the bulk plasmon energy is selected for the reconstruction. Bulk plasmon maps are generated at an energy loss of 15 eV. The width of the energy slit is 3 eV. A HAADF–STEM tilt series is also acquired from the same sample for comparison. For the HAADF–STEM tilt series, an incremental angle of 2° is used between two projections. In Fig. 6 a 2D bulk plasmon map is compared to a HAADF–STEM projection. The intensity profile reveals that diffraction contrast is still present in the bulk plasmon map, whereas the contrast in the HAADF–STEM projection is only related to the thickness of the sample. A reconstruction for both techniques is made using the SIRT algorithm and voltex visualisations are shown in Fig. 7. The morphology is well reconstructed by both techniques, but fanning effects are present in the orthoslice

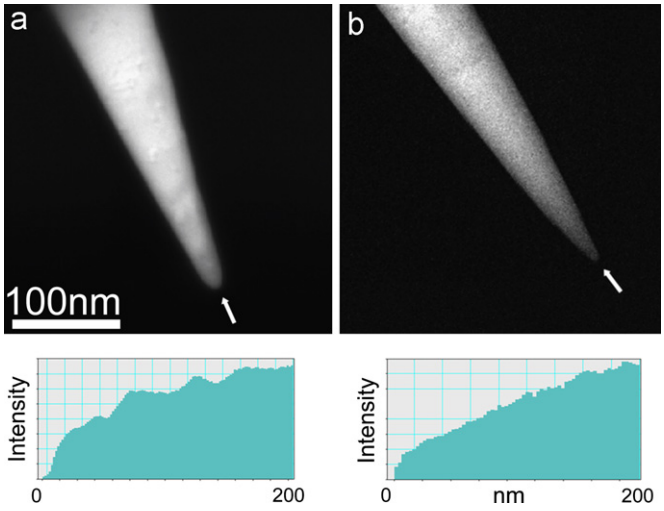

Fig. 6. Comparison of a bulk plasmon map (a) to a HAADF–STEM projection (b) of an Al needle-shaped specimen. The intensity profile is in both cases chosen in the direction of the white arrow. The intensity profile in the HAADF–STEM image thickness contrast which shows that the HAADF–STEM images fulfil the projection requirement. The intensity profile of the bulk plasmon map shows some diffraction contrast where there is no monotonic function between the intensity in the projection and the thickness of the sample.

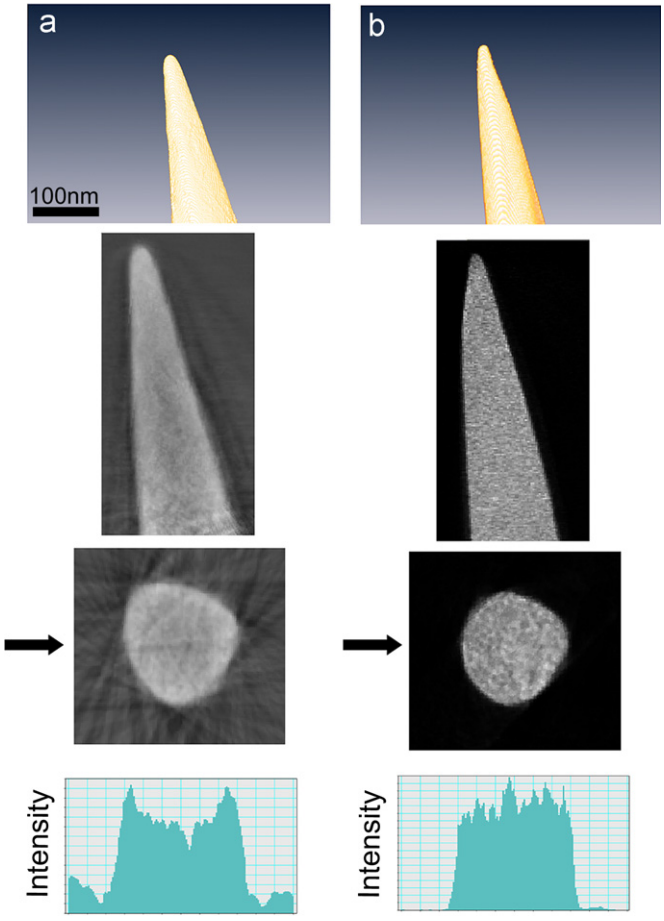

Fig. 7. Reconstruction of the Al needle-shaped specimen. The reconstruction is based on a bulk plasmon map tilt series (a) and on a HAADF–STEM tilt series (b). The morphology is well reconstructed in both cases, but the orthoslices through the reconstruction show some fanning artefacts in the case of bulk plasmon maps. Those fanning artefacts are caused by the large tilt angle between two successive projections. Effects of the diffraction contrast in the bulk plasmon maps can be seen in the intensity profile through the orthoslices. The intensity profile is chosen as indicated by the black arrow in the orthoslice and shows a higher intensity at the side of the reconstruction than at the centre.

through the bulk plasmon reconstruction. These artefacts are caused by the larger angular increment between two successive images in the tilt series. In addition, the intensity profile obtained across the orthoslice shows that the intensity is not uniformly distributed in the case of the bulk plasmon reconstruction, which can be understood because of the residual diffraction contrast present in the 2D bulk plasmon maps. When different materials have a different bulk plasmon energy, bulk plasmon mapping can also be used to selectively visualise one of the materials. A restriction to this is that the surface plasmon energy of one material may not overlap with the bulk plasmon energy of the other material.

4. Discussion

In this study different inelastic imaging techniques are evaluated concerning their use for 3D reconstructions. All techniques are also compared to HAADF–STEM tomography. In HAADF–STEM images, the intensity is proportional to the thickness of the specimen and approximately to the square of the atomic number Z. The technique also yields chemical information, albeit only relative. An inner collection angle of 60 mrad is used in order to reduce diffraction contrast, but at the same time, these settings result in a very high contrast between the Cu core and the C shell of the nanohorn, resulting in an invisible shell in 2D and 3D imaging.

3D information on the absolute chemical composition of a specimen can be obtained by EFTEM, which is the conventional technique when using inelastically scattered electrons for tomography. Both jump ratio maps based on the jump ratio method and elemental maps created with the three window method can be extended to 3D. Because of the multiple images involved to obtain one of these maps, this technique can only be used for specimens that are stable under the electron beam. EFTEM series are usually recorded with larger tilt increment between two successive projections in comparison to HAADF–STEM tilt series. Obviously, this will negatively influence the resolution of the final reconstruction. Elemental maps created by the three window method fulfil the projection requirement as the intensity per pixel rises as more electrons have made a specific excitation. However, residual diffraction contrast caused by elastic scattering is still present in the elemental map. This diffraction contrast can, in principle, be removed using the jump ratio method. It must also be noted that the projection requirement is only fulfilled until thicknesses where multiple scattering becomes important. Disadvantages of jump ratio maps are the poor signal to noise ratio caused by the computational division required to create the jump ratio map and the fact that the projection requirement is not fulfilled. In this study we compared HAADF–STEM reconstructions with reconstructions based on the jump ratio method as well as the three window technique. It is clear that the C shell, which is not visible in the HAADF–STEM reconstruction can be imaged in 3D by the EFTEM reconstruction based on the three window technique. Also the morphology of the Cu core of the nanostructure is very well reconstructed. It should be noted that a combination of remaining diffraction contrast and multiple scattering results in a decrease of the intensity in the inner part of the 3D reconstruction. This should be taken into account when quantification of the 3D reconstruction is carried out. Although jump ratio maps do not fulfil the projection requirement, a 3D reconstruction was carried out based on the tilt series we collected. The most apparent problem in these reconstructions seems to be the poor signal to noise ratio. It is likely that the decrease in intensity in this case is related to the fact that the jump ratio maps (in which diffraction contrast is eliminated) do not carry any thickness information. As shown by Saghi et al. [32], this means that the jump ratio method can be used only to reconstruct the morphology (i.e. convex hull) of a sample. It should be pointed out that a jump ratio map only requires 2 images to form a 2D projection, whereas in the three window technique, 3 images are required. This means that a lower electron dose is required for reconstructions based on the jump ratio method.

A new and promising method that was found to be suitable for 3D reconstructions is thickness mapping based on the log-ratio method. These thickness maps are acquired by dividing a BF-TEM image by a zero-loss image. This technique requires 2 images, which can be obtained using short acquisition times (1.8 s in our case). This method not only succeeds to reconstruct the surface, but also the inner part of nanostructures. Unfortunately, the differences in inelastic free mean path of electrons between different chemical compositions are too small to result in a clear distinction of those chemical compositions in 3D.

Finally, we also compared bulk plasmon tomography with HAADF–STEM tomography. A disadvantage of bulk plasmon tomography is that there is a slight effect of diffraction contrast present in the final 3D reconstruction. On the other hand, the morphology of the sample was well reconstructed. It must also be noted that the large impact parameter for a bulk plasmon excitation will negatively influence the resolution attainable in the final reconstruction [17].

The results of our study are summarised in Table 1, which can be used as a guideline when investigating nanostructures in 3D. From this table, it is clear that all techniques have advantages and disadvantages. Depending on the sample and the information required, the most promising technique for 3D reconstruction can be selected. A reconstruction made by HAADF–STEM tomography produces the best signal to noise ratio, but it is difficult to distinguish different chemical elements either when the contrast in the projections is too large or when the elements have neighbouring Z numbers. By making use of EFTEM tomography, a separate reconstruction can be made for every chemical element, but diffraction contrast present in the elemental map and long acquisition times limit the quality of the reconstruction. A faster acquisition can be achieved using a tilt series of thickness maps. In combination with tomography, those thickness maps can be used for a good reconstruction of the morphology of the specimen. Although diffraction contrast is still present, bulk plasmon tomography can be useful to reconstruct the morphology of samples with a very clear plasmon peak.

Table 1
Overview of the different inelastic projection methods used in this work with their main advantages and disadvantages.

	Electron dose	SNR	Diffraction contrast	Morphology	Chemical elements	Ease of use	Thickness limit	Resolution
HAADF–STEM	±	+	+	+	±	±	+	+
Three window method	−	±	−	+	+	−	±	±
Jump ratio method	−	−	±	−	+	−	±	±
Thickness map	+	±	+	+	−	+	±	+
Bulk plasmon map	−	±	−	+	±	±	±	−

5. Conclusions

We have compared 3D reconstructions based on different inelastic imaging modes in TEM. All reconstructions are also compared to HAADF–STEM as this can be considered as the standard technique for 3D reconstruction in materials science. As a result, in Table 1, we present an overview that can be used to select the best inelastic signal for tomography, depending on the beam stability and nature of the sample, as well as on the exact information which is expected from the 3D reconstruction.

Acknowledgment

The work was supported by the Flemish Fund for Scientific Research (F.W.O. Vlaanderen) through project fundings (G.0247.08, G.0180.08 and G.0147.06) and a PhD research grant to B.G. Financial support of the IAP-PAI network from the Belgian Government is highly appreciated. The authors acknowledge financial support from the European Union under the Framework 6 program under a contract for an Integrated Infrastructure Initiative. Reference 026019 ESTEEM. W. Van den Broek is working under the Condor project, a project under the supervision of the Embedded Systems Institute (ESI) and with FEI company as the industrial partner. This project is partially supported by the Dutch Ministry of Economic Affairs under the BSIK programme. We also thank Prof. X.B. Zhang and Dr. Y. Li for providing the samples.

References

[1] Ph. Buffat, J.-P. Borel, Size effect on the melting temperature of gold particles, Phys. Rev. A 13 (1976) 2287–2298.
[2] W. Hoppe, R. Langer, G. Knesch, Ch. Poppe, Protein-Kristallstrukturanalyse mit Elektronestrahlen, Naturwissenschaften 55 (1968) 333–336.
[3] D.J. De Rosier, A. Klug, Reconstruction of three dimensional structures from electron micrographs, Nature 217 (1968) 130–134.
[4] P.W. Hawkes, The electron microscope as a structure projector, in: J. Frank (Ed.), Electron Tomography: Three Dimensional Imaging with the Transmission Electron Microscope, Plenum Press, New York, 1992, pp. 17–37.
[5] G. Möbus, B.J. Inkson, Three-dimensional reconstruction of buried nanoparticles by element-sensitive tomography based on inelastically scattered electrons, Appl. Phys. Lett. 79 (2001) 1369–1371.
[6] G. Möbus, R.C. Doole, B.J. Inkson, Spectroscopic electron tomography, Ultramicroscopy 96 (2003) 433–451.
[7] P.A. Midgley, M. Weyland, 3D electron microscopy in the physical science: the development of *Z*-contrast and EFTEM tomography, Ultramicroscopy 96 (2003) 413–431.
[8] M. Weyland, P.A. Midgley, Extending energy-filtered transmission electron microscopy (EFTEM) into three dimensions using electron tomography, Microsc. Microanal. 9 (2003) 542–555.
[9] M. Weyland, T.J.V. Yates, R.E. Dunin-Borkowski, L. Laffont, P.A. Midgley, Nanoscale analysis of three-dimensional structures by electron tomography, Scr. Mater. 55 (2006) 29–33.
[10] K. Yamauchi, K. Takahashi, H. Hasegawa, Microdomain morphology in an ABC 3-Miktoarm star terpolymer: a study by energy-filtering TEM and 3D electron tomography, Macromolecules 36 (2003) 6962–6966.
[11] M.H. Gass, K.K. Kozoil, A.H. Windle, P.A. Midgley, Four-dimensional spectral tomography of carbonaceous nanocomposites, Nano. Lett. 6 (2006) 376–379.
[12] A. Yurtsever, M. Weyland, D.A. Muller, Three-dimensional imaging of non-spherical silicon nanoparticles embedded in silicon oxide by plasmon tomography, Appl. Phys. Lett. 89 (2006) 151920.
[13] P.A. Midgley, R.E. Dunin-Borkowski, Electron tomography and holography in materials science, Nat. Mater. 8 (2009) 271–280.
[14] C. Kubel, A. Voigt, R. Schoenmakers, M. Otten, D. Su, T.-C. Leem, A. Carlsson, J. Bradley, Recent advances in electron tomography: TEM and HAADF-STEM tomography for materials science and semiconductor applications, Microsc. Microanal. 11 (2005) 378–400.
[15] J.M. Thomas, P.A. Midgley, T.J.V. Yates, J.S. Barnard, R. Raja, I. Arslan, M. Weyland, The chemical application of high-resolution electron tomography: bright field or dark field?, Angew. Chem. Int. Ed. Engl. 43 (2004) 6745–6747.
[16] R.F. Egerton, Electron Energy Loss Spectroscopy in the Electron Microscope, 2nd ed., Plenum Press, New York, 1996.
[17] H.R. Daniels, R. Brydson, A. Brown, B. Rand, Quantitative valence plasmon mapping in the TEM: viewing physical properties at the nanoscale, Ultramicroscopy 69 (2003) 547–558.
[18] X.Y. Tao, X.B. Zhang, J.P. Cheng, F. Liu, Synthesis and characterization of Cu filled carbon nanohorns, Mater. Chem. Phys. 104 (2007) 210–214.
[19] P. Gilbert, Iterative methods for the three-dimensional reconstruction of an object from projections, J. Theor. Biol. 36 (1972) 105–107.
[20] P.A. Crozier, Quantitative elemental mapping of materials by energy-filtered imaging, Ultramicroscopy 58 (1995) 157–174.
[21] F. Hofer, W. Grogger, G. Kothleitner, P. Warbichler, Quantitative analysis of EFTEM elemental distribution images, Ultramicroscopy 67 (1997) 83–103.
[22] M. Weyland, P.A. Midgley, Electron tomography, in: A. Kirkland, J.L. Hutchison (Eds.), Nanocharacterisation, RSC Publishing, Cambridge, 2007, pp. 184–259.
[23] P.A. Crozier, Measurement of inelastic electron scattering cross-sections by electron energy-loss spectroscopy, Phil. Mag. B 61 (1991) 311–336.
[24] D.R. Mitchell, Determination of mean free path for energy loss and surface oxide film thickness using convergent beam electron diffraction and thickness mapping: a case study using Si and P91 steel, J. Microsc. 224 (2006) 187–196.
[25] R.F. Egerton, S.C. Cheng, Measurement of local thickness by electron energy-loss spectroscopy, Ultramicroscopy 21 (1987) 231–244.
[26] S. Bals, J.K. Batenburg, J. Verbeeck, J. Sijbers, G. Van Tendeloo, Quantitative three-dimensional reconstruction of catalyst particles for bamboo-like C Nanotubes, Nano. Lett. 7 (2007) 3669–3674.
[27] K. Iakoubovskii, K. Mitsuishi, Y. Nakayama, K. Furuya, Mean free path of inelastic electron scattering in elemental solids and oxides using transmission electron microscopy: atomic number dependent oscillatory behavior, Phys. Rev. B 77 (2008) 104102.
[28] Y. Li, H. Tan, X.-Y. Yang, B. Goris, J. Verbeeck, S. Bals, P. Colson, G. Van Tendeloo, B.-L. Su, Well shaped Mn_3O_4 nano-octahedra with anomalous magnetic behavior and enhanced photodecomposition properties, Small 7 (2011) 475–483.
[29] X. Ke, S. Bals, D. Cott, T. Hantschel, H. Bender, G.Van Tendeloo, Three-dimensional analysis of carbon nanotube network in interconnects by electron tomography without missing wedge artifacts, Microsc. Microanal. 16 (2010) 210–217.
[30] N. Kawase, M. Kato, H. Nishioka, H. Jinnai, Transmission electron microtomography without the "missing wedge" for quantitative structural analysis, Ultramicroscopy 107 (2007) 8–15.
[31] J.-L. Lavergne, J.-M. Martin, M. Belin, Interactive electron energy-loss elemental mapping by the "Imaging-Spectrum" method, Microsc. Microanal. Microstruct. 3 (1992) 517–528.
[32] Z. Saghi, X. Xu, G. Möbus, Electron tomography of regularly shaped nanostructures under non-linear image acquisition, J. Microsc. 2332 (2008) 186–195.